

Article

High Efficiency Dual-Active-Bridge Converter with Triple-Phase-Shift Control for Battery Charger of Electric Vehicles

Shih-hao Kuo ^{1,*}, Huang-Jen Chiu ¹, Che-Wei Chiang ¹, Ta-Wei Huang ¹, Yu-Chen Chang ¹, Serafin Bachman ² , Szymon Piasecki ² , Marek Jasinski ²  and Marek Turzyński ³ 

¹ Department of Electronic and Computer Engineering, National Taiwan University of Science and Technology, Taipei 106, Taiwan

² Institute of Control and Industrial Electronics, Warsaw University of Technology, 00-662 Warsaw, Poland

³ Faculty of Electrical and Control Engineering, Gdańsk University of Technology, 80-233 Gdansk, Poland

* Correspondence: d10502202@mail.ntust.edu.tw; Tel.: +886-918-746-938

Abstract: An optimal modulation scheme with triple-phase-shift (TPS) control could increase the efficiency in the entire load range for a dual-active-bridge (DAB) converter under wide output voltage range conditions. Therefore, this study proposes a convergent approach to TPS mode selection, coupled with an optimal modulation scheme, ensuring the circuit's efficiency over the entire range in the realm of a high-power and high-efficiency battery charger for electric vehicles. The convergent approach to TPS mode selection also reduces the numerous cases for small-signal analysis through general average modeling. After verifying the small-signal models under various voltage transfer ratios and load conditions to verify the stability, a converter prototype with a rated power of 15 kW is built and tested. Thus, a peak efficiency of 97.7% can be achieved.

Keywords: dual-active-bridge converter; triple-phase-shift control; small signal; general average modeling



Citation: Kuo, S.-h.; Chiu, H.-J.; Chiang, C.-W.; Huang, T.-W.; Chang, Y.-C.; Bachman, S.; Piasecki, S.; Jasinski, M.; Turzyński, M. High Efficiency Dual-Active-Bridge Converter with Triple-Phase-Shift Control for Battery Charger of Electric Vehicles. *Energies* **2024**, *17*, 354. <https://doi.org/10.3390/en17020354>

Academic Editor: Alon Kuperman

Received: 17 November 2023

Revised: 25 December 2023

Accepted: 8 January 2024

Published: 10 January 2024



Copyright: © 2024 by the authors. Licensee MDPI, Basel, Switzerland. This article is an open access article distributed under the terms and conditions of the Creative Commons Attribution (CC BY) license (<https://creativecommons.org/licenses/by/4.0/>).

1. Introduction

In response to environmental concerns, the rapid expansion of electric vehicles (EVs) is poised to become a major influencer in the global transformation of transportation energy. With the increasing proliferation of electric vehicles, the demand for fast charging is gradually rising. Advanced charging technologies for next-generation electric vehicles have become increasingly attractive for academia and the transportation industry in recent years [1,2].

In the realm of electric vehicle charging, the charge power level is continuously escalating, transitioning from conventional AC charging stations to DC fast charging, with future aspirations set on DC ultra-fast charging. Efficient DC-DC converters play a pivotal role in the realm of electric vehicles, serving as crucial components to enhance overall system performance.

Within the current landscape of electric vehicles, they serve not only as environmentally friendly modes of transportation but also incorporate energy-sharing systems (V2H, V2V or V2G) [3,4]. Importantly, different electric vehicles utilize batteries with varying voltage levels, ranging from a minimum of 200 V to as high as 750 V [5]. Consequently, the design of DC-DC converters in the charging stations must be capable of accommodating a wide range of input and output voltages, as well as bidirectional power functionalities.

High efficiency bidirectional DC-DC converters with a wide voltage range operation are necessary to meet requirements of environment friendliness. The selection of an appropriate converter topology is crucial [6–8]. Among the myriad of DC-DC converters, there exist two distinct types: isolated and non-isolated [9]. Isolated converters offer high

galvanic isolation, and a transformer changes the ratio so that they can be adjusted for a broader voltage output range, in comparison to resonant LLC full-bridge circuits or phase-shift full-bridge circuits, among others [10]. The dual-active-bridge converter provides advantages such as bidirectional power flow control, simplified control methodology, wide-range adjustable voltage output and a reduced number of passive components, making it more advantageous [11–14].

The basic control method of the dual-active-bridge converter involves adjusting the output voltage and power through phase-shift angle control. The single-phase-shift (SPS) modulation stands out as the simplest, involving only one control variable. Consequently, for each determined transmission power, there exists only one corresponding control variable. As a result, the value of circuit's peak value and root-mean-square (RMS) current are also uniquely determined. In the performance evaluation of DAB used in electric vehicles, as discussed in [15], it is observed that even with only some switches entering zero voltage switching (ZVS), the converter can still achieve 96% efficiency under a 10 kW output scenario.

Furthermore, in the application of single-phase-shift control, aside from the reactive power leading to transmission losses from the primary side to the secondary side, when the voltage transfer ratio is not equal to 1, it will result in a constrained range of zero voltage switching in the converter and an increase in both peak and RMS current [16–18]. On the contrary, other control methods such as extended-phase-shift (EPS) modulation, dual-phase-shift (DPS) modulation and triple-phase-shift (TPS) modulation are introduced to address issues related to reactive power at different output voltage ranges, achieve a broader range of zero voltage switching or reduce both peak and RMS current in the DAB converter [19–21].

Among the various control modulation techniques (SPS, EPS, DPS and TPS) applied to the dual-active-bridge converter, in addition to the analysis of the control methods in the time domain, the analysis of the frequency domain for each individual control technique is equally crucial. Small-signal models for frequency domain analysis are pivotal for assessing the stability of the circuit's frequency response, transient response, and guiding the design direction of the circuit controller [22,23].

Based on the presented analysis, the application of control modulation techniques to the dual-active-bridge converter will prompt the introduction of both time-domain and frequency-domain analyses. Through the implementation of various control techniques, it will be verified whether the circuit demonstrates improved efficiency across a broad output range. Additionally, an optimal control scheme based on existing control methods will be proposed, their operational range analyzed, and their small-signal accuracy validated. The circuit will be designed to closely align with the voltage range of contemporary electric vehicle batteries, ensuring a performance evaluation that closely mirrors practical applications. Finally, a 15 kW prototype will be implemented to validate the proposed approaches.

2. Dual-Active-Bridge Converter

The dual-active-bridge converter topology and the phase shift angle between power switches are defined in Figure 1. The duty cycle of each switch is 50%, and the logic of the two switches in the same leg is complementary. D_1 is the duty of the primary voltage V_p on the primary side, corresponding to the phase shift angle between switches Q_1 and Q_3 . D_2 is the duty on the secondary voltage V_s of the secondary side, corresponding to the phase shift angle between switches Q_5 and Q_7 . D_ϕ is the phase shift between the center points of D_1 and D_2 . D_3 is the time difference between the rising edges of V_p and V_s , corresponding to the phase shift between switches Q_1 and Q_5 . The definition of the voltage transfer ratio M is shown in (1).

$$M = N \frac{V_o}{V_{in}} \quad (1)$$

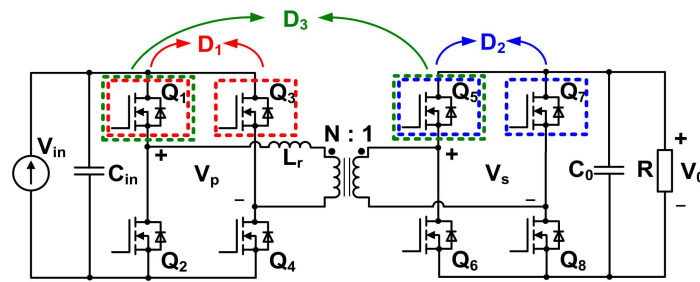


Figure 1. DAB converter and the definition of phase shift.

Each phase shift is defined as the ratio of the phase shift angle θ_x to a period 2π , as shown in (2). The relationship between phase shift D_3 and other phase shifts is shown in (3), and the timing diagram is presented in Figure 2.

$$D_x = \frac{\theta_x}{2\pi}, x = 1, 2, 3, \varphi \quad (2)$$

$$D_3 = D_\varphi + \frac{D_1}{2} - \frac{D_2}{2} \quad (3)$$

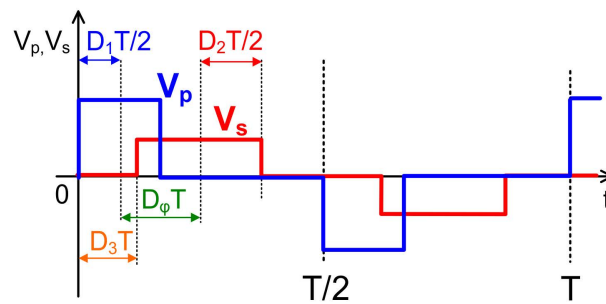


Figure 2. Timing diagram of V_p and V_s waveforms.

Numerous studies have presented various approaches to phase-shift control, such as single-phase-shift (SPS) control, extend-phase-shift (EPS) control, dual-phase-shift (DPS) control, and notably, triple-phase-shift (TPS) control [21–32]. TPS offers various phase-shift control combinations through the control of D_1 , D_2 and D_φ . Some of these combinations can extend the range of zero voltage switching on both the primary and secondary sides, consequently increasing efficiency. Other combinations can reduce the RMS current of the circuit, thereby improving conduction and switching losses in the circuit [21,27,31,32].

Despite the numerous advantages offered by TPS, its practical application necessitates the implementation of a closed-loop controller to regulate the output voltage. Based on [33,34], this study analyzes small signals to achieve precise control of their transient response and introduces a small-signal modeling method called Generalized Average Modeling (GAM) to derive the open-loop power-stage transfer function for a closed-loop controller design.

Due to TPS having various phase shift combinations of D_1 , D_2 , and D_φ at same output power condition, a specific target must be set before the design, and a suitable operation mode must be selected for the analysis [21,32]. The foundation of each TPS operation mode can be referred to as the operation mode analyzed in [21,27,31,32]. Table 1 shows the relationship and definition between the name of each operation mode and its corresponding phase shift under a positive power flow.

To simplify the multiple selection of these operation mode, which need to be analyzed to obtain its output power function, RMS current and switching points current are used.

Table 1. Definition of each operation mode of TPS.

<i>SM_i</i>	<i>Case 1</i>	<i>Case 2</i>
SM1	$0 < D_\varphi \leq \left(\frac{D_1-D_2}{2}\right)$	$0 < D_\varphi \leq \left(\frac{D_2-D_1}{2}\right)$
SM2	$\left(\frac{D_1-D_2}{2}\right) < D_\varphi \leq \left(\frac{D_1+D_2}{2}\right)$	$\left(\frac{D_2-D_1}{2}\right) < D_\varphi \leq \left(\frac{D_2+D_1}{2}\right)$
SM2*	$\left(\frac{D_1-D_2}{2}\right) < D_\varphi \leq \left(1 - \frac{D_1+D_2}{2}\right)$	$\left(\frac{D_2-D_1}{2}\right) < D_\varphi \leq \left(1 - \frac{D_2+D_1}{2}\right)$
SM3	$\left(\frac{D_1+D_2}{2}\right) < D_\varphi \leq \left(1 - \frac{D_1+D_2}{2}\right)$	$\left(\frac{D_2+D_1}{2}\right) < D_\varphi \leq \left(1 - \frac{D_2+D_1}{2}\right)$
SM3*	$\left(1 - \frac{D_1+D_2}{2}\right) < D_\varphi \leq \left(\frac{D_1+D_2}{2}\right)$	$\left(1 - \frac{D_2+D_1}{2}\right) < D_\varphi \leq \left(\frac{D_2+D_1}{2}\right)$
SM4	$\left(1 - \frac{D_1+D_2}{2}\right) < D_\varphi \leq \left(1 - \frac{D_1-D_2}{2}\right)$	$\left(1 - \frac{D_2+D_1}{2}\right) < D_\varphi \leq \left(1 - \frac{D_2-D_1}{2}\right)$
SM5	$\left(1 - \frac{D_1-D_2}{2}\right) < D_\varphi \leq 1$	$\left(1 - \frac{D_2-D_1}{2}\right) < D_\varphi \leq 1$

This study adopted an optimized control method [21,32], entering ZVS mode during light loads to eliminate switching losses. As the output current increases, efforts are directed towards minimizing the circuit’s RMS current to optimize conduction losses. Through this control method, the computational complexity of numerous modes in TPS is simplified, along with reducing the computational burden on the controller. The dedicated power range P_{o1} , which determines whether to adopt ZVS mode, is shown in (4).

$$P_{o1} = \left[\begin{array}{l} \frac{V_{in}^2 M^2 (1-M)}{4L f_s}, M < 1 \\ \frac{V_{in}^2 (M-1)}{4L f_s M}, M > 1 \end{array} \right] \tag{4}$$

When the output power range is $P \in [0, P_{o1}]$, DAB will operate in SM1 (ALL-ZVS mode), and when the output power range is $P \in [P_{o1}, M\pi/4]$, DAB will operate in SM3* (Minimum Peak Current mode). The optimized phase shift variables, D_1 , D_2 and D_φ , are shown in Table 2 and are, respectively, labeled according to the voltage conversion ratio M and switching waveform shown in Figure 3. The goal is to achieve ZVS for all switches under light load conditions so that TPS operates in SM1. Table 3 shows the required switching point current, which can achieve ZVS.

Table 2. Optimized phase shift angle value.

<i>Power Range</i>	<i>M</i>	<i>M < 1</i> <i>(Case 2)</i>	<i>M > 1</i> <i>(Case 1)</i>
$P \in [0, P_{o1}]$		$D_{1_opt} = \sqrt{\frac{2P_o}{(1-M)\pi}}$	$D_{1_opt} = \frac{1}{M} \sqrt{\frac{2P_o}{M(M-1)\pi}}$
		$D_{2_opt} = \sqrt{\frac{2P_o}{M^2(1-M)\pi}}$	$D_{2_opt} = \sqrt{\frac{2P_o}{M(M-1)\pi}}$
		$D_{\varphi_opt} = \sqrt{\frac{2(1-M)\pi P_o}{2\pi M}}$	$D_{\varphi_opt} = \sqrt{\frac{2P_o(M-1)}{M\pi}}$
$P \in [P_{o1}, M\pi/4]$		$D_{1_opt} = 1 - (1-M) \sqrt{\frac{M\pi - 4P_o}{(1-2M+2M^2)M\pi}}$	$D_{1_opt} = 1$
		$D_{2_opt} = 1$	$D_{2_opt} = 1 - \sqrt{\left(1 - \frac{4P_o}{M\pi}\right) \frac{(M-1)^2}{(M-1)^2 + 1}}$
		$D_{\varphi_opt} = 0.5 - 0.5 \sqrt{\frac{M(M\pi - 4P_o)}{(1-2M+2M^2)\pi}}$	$D_{\varphi_opt} = 1 - \sqrt{2D_{2_opt} - D_{\varphi_opt}^2 - \frac{4P_o}{M\pi}}$

TPS has the most remarkable effect on improving the reactive power, current peak value and RMS value because of its diversity and capability of providing a larger ZVS range and wider voltage conversion ratio, making it possible to achieve ZVS under light load conditions. The drawback of TPS is its complexity in control. With the optimal control method for selecting limited modes in TPS, the number of modes requiring analysis has been reduced. In this study, a small-signal model analysis of TPS within the optimal

operational range was proposed. The obtained results focus on analyzing specific modes (*Case 1 SM1*, *Case 2 SM1*, *Case 1 SM3** and *Case 2 SM3**), but the approach can still be broadly applied to other TPS modes. Utilizing the analysis results, a compensator can be designed to assess loop stability through a bode plot. In practical experiments, an Ambiguous mode needs to be applied between the ALL-ZVS mode and the Minimum Peak Current mode to ensure a smooth transient response.

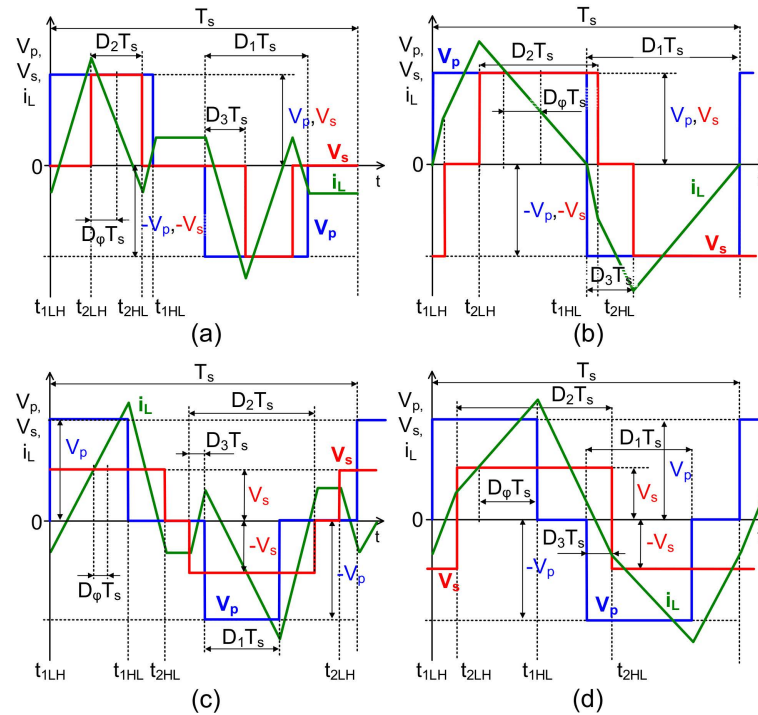


Figure 3. Timing diagram of TPS, (a) *Case 1 SM1*, (b) *Case 1 SM3**, (c) *Case 2 SM1*, (d) *Case 2 SM3**.

Table 3. ZVS conditions of *SM1*.

Switches	ZVS Conditions
Q_1	$i_{L(t_{1LH})} \leq I_{\min_Q1} \left(-\sqrt{\frac{2V_{in}^2 C_{oss} (1-2M)}{L}} \right)$
Q_3	$i_{L(t_{1HL})} \leq I_{\min_Q3} \left(\sqrt{\frac{2V_{in}^2 C_{oss} (1-2M)}{L}} \right)$
Q_5	$i_{L(t_{2LH})} \leq I_{\min_Q5} \left(\sqrt{\frac{2V_{in}^2 C_{oss}}{L}} \right)$
Q_7	$i_{L(t_{2HL})} \leq I_{\min_Q7} \left(-\sqrt{\frac{2V_{in}^2 C_{oss}}{L}} \right)$

3. Small-Signal Modeling and Analysis of TPS

In the conventional state–space averaging method, the state variables of the circuit (e.g., output capacitor voltage and inductor current) are averaged, The AC components are ignored and calculated as pure DC values. This method is suitable for a topology with a small AC component, but the inductor current in DAB is pure AC. If the traditional state–space averaging method is applied, then the state cannot be accurately represented; thus, the generalized state–space averaging method must be used [33]. The definition of the state–space model to be used is shown in (5), and the *A*, *B*, *C* and *D* matrices are the targets of the derivation.

$$\begin{aligned} \dot{x}_s &= Ax_s + Bu_s \\ y_s &= Cx_s + Du_s \end{aligned} \tag{5}$$

Next, the state variable matrix x_s , the output variable matrix y_s and the input variable matrix u_s required for the derivation are defined, and their included variables are shown in (6).

$$x_s = \begin{bmatrix} \Delta v_c \\ \Delta i_{L_1R} \\ \Delta i_{L_1I} \\ \Delta v_o \\ 0 \end{bmatrix} \quad u_s = \begin{bmatrix} \Delta d_1 \\ \Delta d_2 \\ \Delta d_\phi \\ \Delta v_{in} \\ \Delta i_N \end{bmatrix} \quad y_s = \begin{bmatrix} \Delta v_o \\ \Delta i_o \\ 0 \\ 0 \\ 0 \end{bmatrix} \quad (6)$$

The switches are assumed to be ideal without resistance $R_{DS(on)}$ to simplify the analysis. The magnetizing inductance L_m of the transformer is regarded as infinite and ignorable. The input is considered an ideal voltage source; thus, the input capacitor C_{in} is ignored. R_t is the sum of the wire resistance of the transformer and the inductor equivalent on the primary side. r_c is the equivalent series resistance (ESR) of the output capacitors. i_N is the disturbance of the output current I_o . The model used for the derivation is shown in Figure 4.

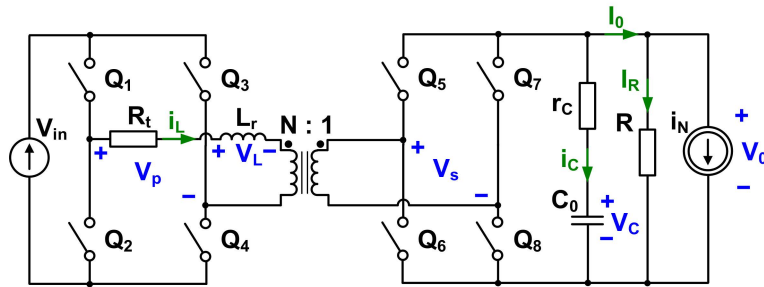


Figure 4. Small-signal model.

Different voltage conversion ratios and load conditions result in various switching sequence and corresponding inductor current shapes. Thus, four operation modes are used in this study, and the derivation details are conducted with *SM1* of *Case 2*. The relationship between V_p, V_s , and the input and output voltages V_{in}, V_o , must be defined in the small-signal model, as shown in (7).

$$\begin{aligned} V_p(t) &= s_1(t) \times V_{in} \\ V_s(t) &= s_2(t) \times V_o \end{aligned} \quad (7)$$

s_1 and s_2 represent the timing of the primary and secondary side switches, respectively. The expression of the waveforms of V_p and V_s in Figure 3c are listed, as shown in (8) and (9), respectively. The period T is the reciprocal of switching frequency f_s .

$$s_1(t) = \begin{pmatrix} 1, & 0 \leq t < D_1 T \\ 0, & D_1 T \leq t < \frac{T}{2} \\ -1, & \frac{T}{2} \leq t < \frac{T}{2} + D_1 T \\ 0, & \frac{T}{2} + D_1 T \leq t < T \end{pmatrix} \quad (8)$$

$$s_2(t) = \begin{pmatrix} 1, & 0 \leq t < D_\phi T + \frac{(D_1+D_2)T}{2} \\ 0, & D_\phi T + \frac{(D_1+D_2)T}{2} \leq t < D_\phi T + \frac{(1+D_1-D_2)T}{2} \\ -1, & D_\phi T + \frac{(1+D_1-D_2)T}{2} \leq t < D_\phi T + \frac{(1+D_1+D_2)T}{2} \\ 0, & D_\phi T + \frac{(1+D_1+D_2)T}{2} \leq t < D_\phi T + \frac{(2+D_1-D_2)T}{2} \\ 1, & D_\phi T + \frac{(2+D_1-D_2)T}{2} \leq t < T \end{pmatrix} \quad (9)$$

Next, according to Kirchhoff’s voltage and current laws, the relationship between inductor voltage and current and that between output capacitor voltage and current, the

relational expression of output voltage, and the relational expression of output current can be listed, as shown in (10)–(13).

$$V_L(t) = L_t \frac{di_L(t)}{dt} = V_p(t) - V_{R_t}(t) - NV_s(t) \quad (10)$$

$$i_c(t) = C_o \frac{dV_c(t)}{dt} = N \times i_L(t) - i_R(t) - i_N(t) \quad (11)$$

$$V_o(t) = \frac{R \times r_c}{R + r_c} \times N \times s_2(t) i_L(t) - \frac{R \times r_c}{R + r_c} \times i_N(t) + \frac{R}{R + r_c} \times V_c(t) \quad (12)$$

$$I_o(t) = \frac{r_c}{R + r_c} \times N \times s_2(t) i_L(t) + \frac{1}{R + r_c} \times V_c(t) + \frac{R}{R + r_c} \times i_N(t) \quad (13)$$

Given that $i_R = V_o/R$, (12) can be used to replace i_R in (13); thus, (14) can be obtained.

$$i_c(t) = C_o \frac{dV_c(t)}{dt} = \frac{NR}{R + r_c} \times i_L(t) s_2(t) - \frac{1}{R + r_c} \times V_c(t) - \frac{R}{R + r_c} \times i_N(t) \quad (14)$$

The four aforementioned equations can be converted into three equations: zero-order, and first-order (one real part and one imaginary part) [28]. The rewritten equations of the first-order real and imaginary parts of i_L are shown in (15) and (16), respectively.

$$\frac{d}{dt} \langle i_L \rangle_{1R} = \frac{-R_t}{L_t} \langle i_L \rangle_{1R} + \omega_s \langle i_L \rangle_{1I} + \frac{1}{L_t} \langle s_1 \rangle_0 \langle v_{in} \rangle_{1R} + \frac{1}{L_t} \langle s_1 \rangle_{1R} \langle v_{in} \rangle_0 - \frac{N}{L_t} \langle s_2 \rangle_0 \langle v_o \rangle_{1R} - \frac{N}{L_t} \langle s_2 \rangle_{1R} \langle v_o \rangle_0 \quad (15)$$

$$\frac{d}{dt} \langle i_L \rangle_{1I} = \frac{-R_t}{L_t} \langle i_L \rangle_{1I} - \omega_s \langle i_L \rangle_{1R} + \frac{1}{L_t} \langle s_1 \rangle_0 \langle v_{in} \rangle_{1I} + \frac{1}{L_t} \langle s_1 \rangle_{1I} \langle v_{in} \rangle_0 - \frac{N}{L_t} \langle s_2 \rangle_0 \langle v_o \rangle_{1I} - \frac{N}{L_t} \langle s_2 \rangle_{1I} \langle v_o \rangle_0 \quad (16)$$

Most of the output capacitor voltage v_c is a DC component, and the proportion of the AC component is relatively small; thus, v_c does not need to consider its first-order real and imaginary terms but only needs to consider its zero-order term.

$$\begin{aligned} \frac{d}{dt} \langle v_c \rangle_0 &= \frac{-R}{C_o(R+r_c)} \langle i_N \rangle_0 - \frac{1}{C_o(R+r_c)} \langle v_c \rangle_0 + \frac{NR}{C_o(R+r_c)} \langle s_2 \rangle_0 \langle i_L \rangle_0 \\ &+ \frac{2NR}{C_o(R+r_c)} \langle s_2 \rangle_{1R} \langle i_L \rangle_{1R} + \frac{2NR}{C_o(R+r_c)} \langle s_2 \rangle_{1I} \langle i_L \rangle_{1I} \end{aligned} \quad (17)$$

As output variables, v_o and i_o do not need to be differentiated, and these are mainly DC components.

$$\langle v_o \rangle_0 = \frac{NRr_c}{R + r_c} \langle s_2 \rangle_0 \langle i_L \rangle_0 + \frac{2NRr_c}{R + r_c} \langle s_2 \rangle_{1R} \langle i_L \rangle_{1R} + \frac{2NRr_c}{R + r_c} \langle s_2 \rangle_{1I} \langle i_L \rangle_{1I} - \frac{Rr_c}{R + r_c} \langle i_N \rangle_0 + \frac{R}{R + r_c} \langle v_c \rangle_0 \quad (18)$$

$$\langle i_o \rangle_0 = \frac{Nr_c}{R + r_c} \langle s_2 \rangle_0 \langle i_L \rangle_0 + \frac{2Nr_c}{R + r_c} \langle s_2 \rangle_{1R} \langle i_L \rangle_{1R} + \frac{2Nr_c}{R + r_c} \langle s_2 \rangle_{1I} \langle i_L \rangle_{1I} + \frac{R}{R + r_c} \langle i_N \rangle_0 + \frac{1}{R + r_c} \langle v_c \rangle_0 \quad (19)$$

The five aforementioned equations reveal several new variables, and some of these variables can be defined to simplify the equation. Assume that the dynamic characteristics of input voltage and load are substantially slower than the dynamic characteristics of DAB. Therefore, the first-order real and imaginary terms of v_{in} and i_o are set to 0, and the zero-order term is its DC value, as shown in (20).

$$\begin{aligned} \langle v_{in} \rangle_{1R} &= \langle v_{in} \rangle_{1I} = 0, \langle v_{in} \rangle_0 = V_{in} \\ \langle i_o \rangle_{1R} &= \langle i_o \rangle_{1I} = 0, \langle i_o \rangle_0 = I_o \end{aligned} \quad (20)$$

Next, the switching signals s_1 and s_2 must be processed using the Fourier series. The timing equations of the switches are integrated to obtain the three coefficients of s_1 and s_2

separately. The calculation only considers the first-order harmonic; thus, the order k in a_1 and b_1 is substituted for 1. The results of s_1 and s_2 are shown in (21) and (22), respectively.

$$\begin{aligned} a_0 &= 0 \\ a_1 &= \frac{2 \sin(2\pi D_1)}{\pi} \\ b_1 &= -\frac{2 \cos(2\pi D_1) - 2}{\pi} \end{aligned} \tag{21}$$

$$\begin{aligned} a_0 &= 0 \\ a_1 &= \frac{2 \sin[\pi(D_1 + D_2 + 2D_\varphi)] - 2 \sin[\pi(D_1 - D_2 + 2D_\varphi)]}{\pi} \\ b_1 &= -\frac{2 \cos[\pi(D_1 + D_2 + 2D_\varphi)] - 2 \cos[\pi(D_1 - D_2 + 2D_\varphi)]}{\pi} \end{aligned} \tag{22}$$

The above results must be averaged using the concept of sliding average to address the changes in the state variables, and the order k is substituted for 1 [34]. The results are arranged to obtain the averaged first-order real and imaginary part coefficients. The results of s_1 and s_2 are shown in (23) and (24), respectively; these results are the same as those of other operation modes.

$$\begin{aligned} \langle s_1 \rangle_{1R} &= \frac{\sin(2\pi D_1)}{\pi} \\ \langle s_1 \rangle_{1I} &= \frac{\cos(2\pi D_1) - 1}{\pi} \end{aligned} \tag{23}$$

$$\begin{aligned} \langle s_2 \rangle_{1R} &= \frac{\sin[\pi(D_1 + D_2 + 2D_\varphi)] - \sin[\pi(D_1 - D_2 + 2D_\varphi)]}{\pi} \\ \langle s_2 \rangle_{1I} &= \frac{\cos[\pi(D_1 + D_2 + 2D_\varphi)] - \cos[\pi(D_1 - D_2 + 2D_\varphi)]}{\pi} \end{aligned} \tag{24}$$

Subsequently, a disturbance is added to each variable, as shown in (25), where the uppercase part and the lowercase with Δ represent its DC and AC small-signal components, respectively.

$$\begin{aligned} D_1 &= D_1 + \Delta d_1 \\ D_2 &= D_2 + \Delta d_2 \\ D_\varphi &= D_\varphi + \Delta d_\varphi \\ \langle v_{in} \rangle_0 &= V_{in_0} + \Delta v_{in_0} \\ \langle v_o \rangle_0 &= V_{o_0} + \Delta v_{o_0} \\ \langle i_L \rangle_{1R} &= I_{L_1R} + \Delta i_{L_1R} \\ \langle i_L \rangle_{1I} &= I_{L_1I} + \Delta i_{L_1I} \\ \langle i_o \rangle_0 &= I_{o_0} + \Delta i_{o_0} \end{aligned} \tag{25}$$

I_{L_1R} and I_{L_1I} are the first-order real and imaginary part coefficients of the inductor current, respectively, and the processing steps are the same as s_{1_1R} and s_{1_1I} . The current definition of each point is shown in Figure 5.

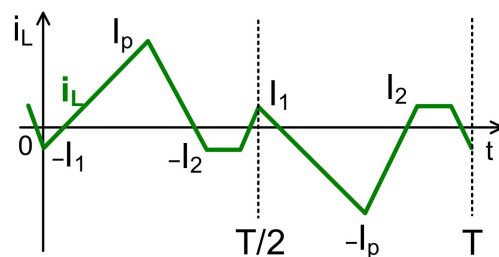


Figure 5. Name of each point of the inductor current.

The point currents I_1 , I_2 and I_p must also be defined. In accordance with the expression of the inductor current of *Case 2 SM1* in each interval, the equation of each point current can be obtained. The results are shown in (26)–(28).

$$I_1 = \frac{2D_1 \left(\frac{V_{in_0}}{N} - V_{o_0} \right) - 4V_{o_0} D_\varphi}{4L_t f_s \frac{1}{N}} \tag{26}$$

$$I_2 = -\frac{2D_1 \frac{V_{in,0}}{N} - 2D_2 V_{o,0}}{4L_t f_s \frac{1}{N}} \tag{27}$$

$$I_p = \frac{2D_1(\frac{V_{in,0}}{N} - V_{o,0}) + 4V_{o,0}D_\varphi}{4L_t f_s \frac{1}{N}} \tag{28}$$

The waveform sequence of the inductor current can then be defined. The inductor current equation and the definition of each time point are shown in (29). The sequence can be processed using the Fourier series to obtain the DC term a_0 and the first-order Fourier coefficients a_1 and b_1 , and the sliding average same is the same as s_{1_1R} and s_{1_1I} . The results of I_{L_1R} and I_{L_1I} are not presented in this study because the equations are too long.

$$i_L(t) = \left\{ \begin{array}{ll} -I_1 + \frac{v_{in} - Nv_o}{L_t} * (t - 0) & , 0 \leq t < t_1 \\ I_p + \frac{0 - Nv_o}{L_t} * (t - t_1) & , t_1 \leq t < t_2 \\ -I_2 + \frac{0 - 0}{L_t} * (t - t_2) & , t_2 \leq t < t_3 \\ -I_2 + \frac{0 - (-Nv_o)}{L_t} * (t - t_3) & , t_3 \leq t < t_4 \\ I_1 + \frac{(-v_{in}) - (-Nv_o)}{L_t} * (t - t_4) & , t_4 \leq t < t_5 \\ -I_p + \frac{0 - (-Nv_o)}{L_t} * (t - t_5) & , t_5 \leq t < t_6 \\ I_2 + \frac{0 - 0}{L_t} * (t - t_6) & , t_6 \leq t < t_7 \\ I_2 + \frac{0 - Nv_o}{L_t} * (t - t_7) & , t_7 \leq t < T \end{array} \right. \tag{29}$$

$$t_1 = D_1 T, t_2 = \frac{(D_1 + D_2)T}{2} + D_\varphi T, t_3 = \frac{(1 + D_1 - D_2)T}{2} + D_\varphi T$$

$$t_4 = \frac{T}{2}, t_5 = \frac{T}{2} + D_1 T, t_6 = \frac{(1 + D_1 + D_2)T}{2} + D_\varphi T$$

$$t_7 = \frac{(2 + D_1 - D_2)T}{2} + D_\varphi T$$

Finally, the small-signal coefficient terms of the variables of each equation in (15)–(19) must be arranged. The results are substituted into (5) and put into matrices A , B , C and D . The detailed elements are presented in Appendix A, specifically labeled from (A1) to (A5). The first Equation (5) is then sorted into the form x_s and entered as y_s . Equation (30) can be obtained after sorting. In this form, different combinations of input variables u_s and output variables y_s can be freely selected to express the relationship between the two variables.

$$\frac{y_s}{u_s} = C(sI - A)^{-1}B + D \tag{30}$$

Next, the result is verified. The phase shifts D_1 and D_2 are calculated through the phase shift D_φ , thus the relationship between Δd_φ and Δv_o is verified. The transfer function is defined as $G_{v\varphi(s)}$, as shown in (31).

$$G_{v\varphi}(s) = \frac{\Delta v_o}{\Delta d_\varphi} = (1 \ 0 \ 0 \ 0 \ 0) \left[C(sI - A)^{-1}B \begin{pmatrix} 0 \\ 0 \\ 1 \\ 0 \\ 0 \end{pmatrix} + D \begin{pmatrix} 0 \\ 0 \\ 1 \\ 0 \\ 0 \end{pmatrix} \right] \tag{31}$$

The output voltage of the phase shift angle transfer function (32) can be obtained after sorting $G_{v\varphi}(s)$. This function contains the PWM modulation gain $F_m(s)$, a simplified second-order formula $K_s(s)$, and one zero, one pole and a set of complex conjugate poles. The zero comprise C_o and its ESR; the pole comprises the load R , C_o and its ESR; and the complex conjugate poles are affected by ω_s .

$$G_{v\varphi}(s) = \frac{F_m(s) \times 4NR \times (sC_o r_c + 1)K_s(s)}{\pi(sC_o r_c + sC_o R + 1)(s^2 L_t^2 + 2sL_t R_t + L_t^2 \omega_s^2 + R_t^2)} \tag{32}$$

The composition of the derivation results of each operation mode (*Case 1 SM1*, *Case 1 SM3**, *Case 2 SM1* and *Case 2 SM3**) is the same as (32). Table 4 shows the circuit parameters. Figure 6 shows the open-loop bode plot of the power stage based on these parameters.

Table 4. Circuit parameter table.

Parameters	Value
Switching Frequency (f_s)	20 kHz
Input Voltage (V_{in})	750 V
Load Resistance (R)	62.5 Ω ($M = 0.5, 1 \text{ kW}$)
	8.33 Ω ($M = 0.5, 7.5 \text{ kW}$)
	562.5 Ω ($M = 1.5, 1 \text{ kW}$)
	37.5 Ω ($M = 1.5, 15 \text{ kW}$)
Output Capacitance (C_o)	560 μF
Output Capacitor ESR (r_c)	50 m Ω
Series Inductance (L_t)	164 μH
Circuit DCR (R_t)	55 m Ω
Turns Ratio (N)	1.55:1
PWM Modulation Gain ($F_m(s)$)	1/3000

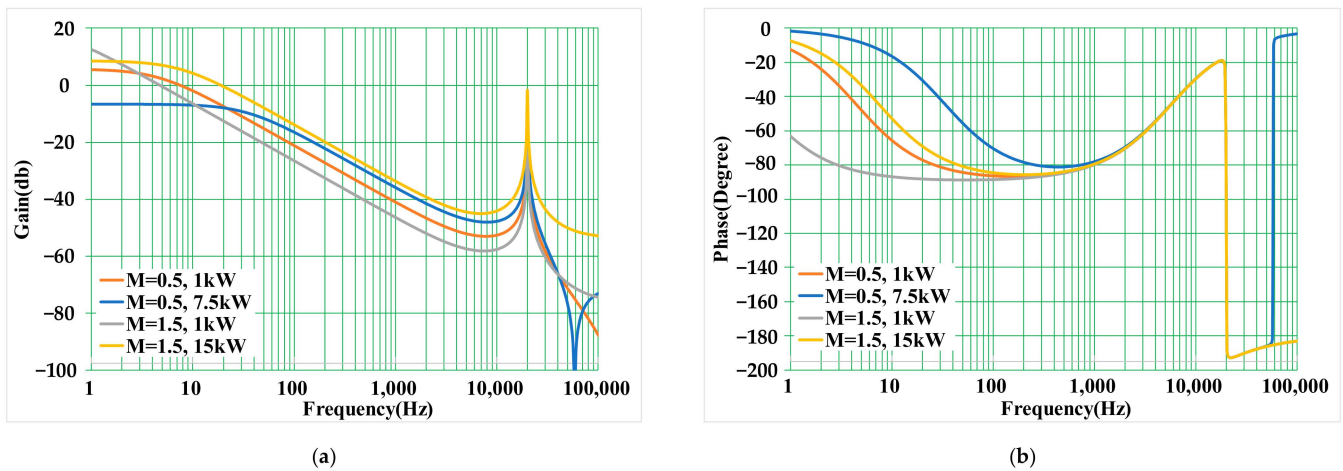


Figure 6. Bode plot of $G_{v\phi}(s)$. (a) Gain, (b) Phase.

4. Control Loop Design Consideration

A high efficiency algorithm must be implemented to achieve the full range of high efficiency operation. In light loads ($P \in [0, P_{o1}]$), DABs with low efficiency due to switching loss will operate in ALL-ZVS mode (*Case 1 SM1* or *Case 2 SM1*). Along with increasing output current ($P \in [P_{o1}, M\pi/4]$), the Minimum Peak Current mode (*Case 1 SM3** or *Case 2 SM3**) must be applied to lower the RMS current. Between the two modes, the Ambiguous mode calculates parameters derived from the equations of both ALL-ZVS mode and Minimum Peak Current mode to resolve the transition. The final output parameter is determined by the solved parameters, specifically D_1 and D_2 , with the greater value taking precedence. However, the situation is reversed for D_ϕ . The system block diagram and the correlation between the phase shift angle and output power are depicted in Figures 7 and 8. The result of the Ambiguous mode calculation is represented by the purple line.

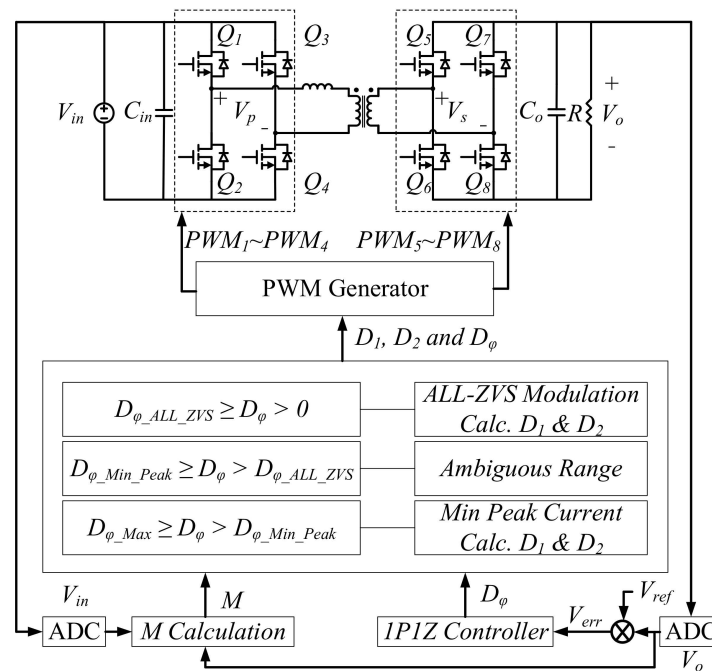


Figure 7. System block diagram.

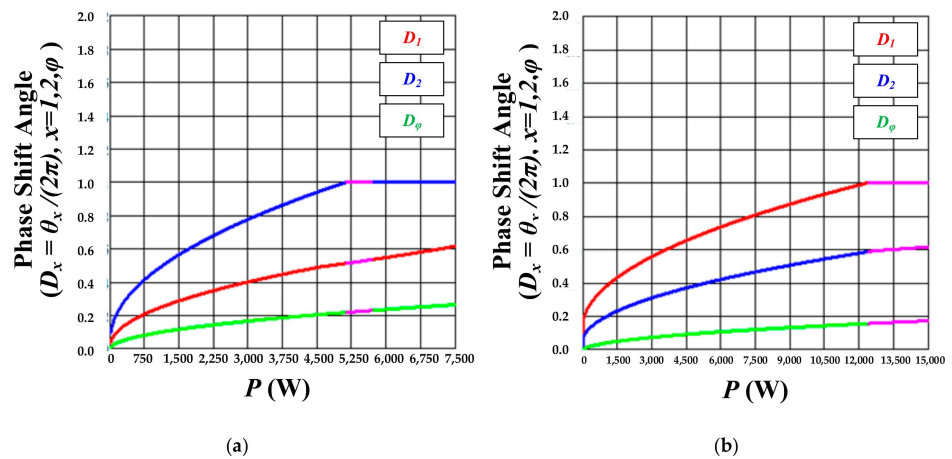


Figure 8. Phase shift angle to output power. (a) $V_o = 250$ V, (b) $V_o = 750$ V.

The closed loop must be implemented to control the output power and voltage. The control loop gain is shown in (33) and (34), and the feedback gain K is 0.002. Meanwhile, the compensator $G_{ea}(s)$ provides one pole and one zero.

$$\frac{\hat{v}_o}{\hat{i}_o} = \frac{-Z_o(s)}{1 + G_{loop}(s)} = \frac{-Z_o(s)}{1 + G_{v\phi}(s) \times K \times G_{ea}(s) \times F_m(s)} \tag{33}$$

$$Z_o(s) = \frac{\Delta v_o}{\Delta i_o} = (1 \ 0 \ 0 \ 0 \ 0) \left[C(sI - A)^{-1}B \begin{pmatrix} 0 \\ 0 \\ 0 \\ 0 \\ 1 \end{pmatrix} + D \begin{pmatrix} 0 \\ 0 \\ 0 \\ 0 \\ 1 \end{pmatrix} \right] \tag{34}$$

Next, the simulation result of the closed-loop $G_{loop}(s)$ Bode plot is shown in Figure 9. The original $M = 0.5$, 7.5 kW condition is limited by sufficient DC gain to regulate the output voltage, which can be solved after compensation. The simulation results only records from 100 Hz to 250 kHz because the full frequency range simulation is time-consuming.

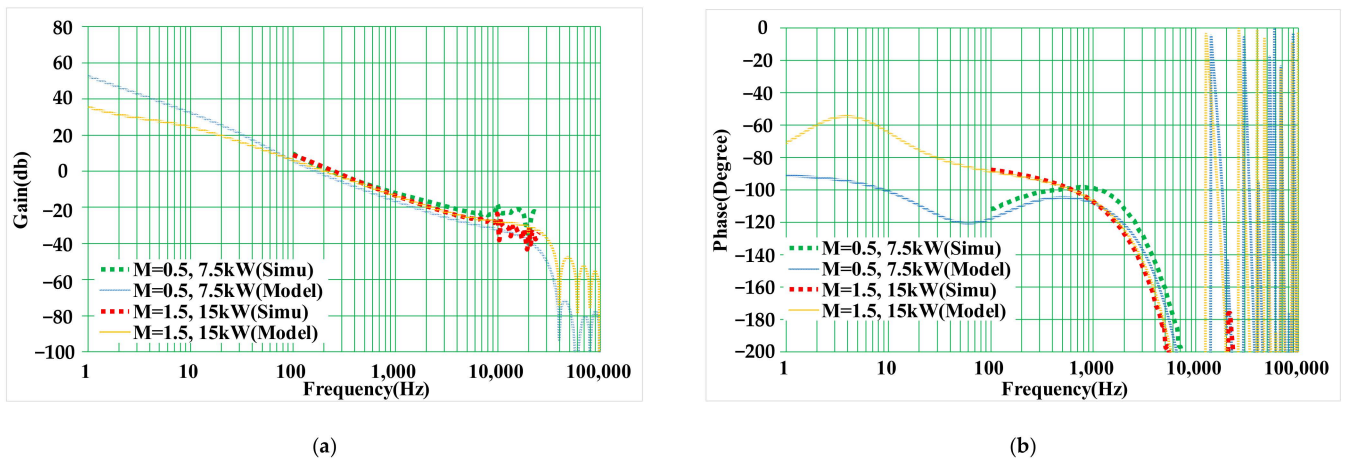


Figure 9. Bode plot of $G_{loop}(s)$. (a) Gain, (b) Phase.

5. Experimental Verifications

Table 5 is the specification parameter table for the DAB converter. The soft-start, transient response and TPS/SPS comparison tests are conducted. Figure 10 illustrates that the output power is constrained by the maximum constant current point and maximum output power, emulating the actual charging behavior of the battery.

Table 5. Specifications parameter table of DAB.

Parameters	Value
Switching Frequency (f_s)	20 kHz
Input Voltage (V_{in})	750 V
Output Voltage (V_o)	250 V~750 V
Maximum Output Power (P_o)	15 kW
Maximum Output Current (I_o)	30 A (Constant Current)
Output Capacitance (C_o)	560 μ F
Output Capacitor ESR (r_c)	50 m Ω
Series Inductance (L_t)	164 μ H
MOSFET Output Capacitance (C_{oss})	550 pF
Turns Ratio (N)	(Infineon FF23MR12W1M1_B11) 1.55:1

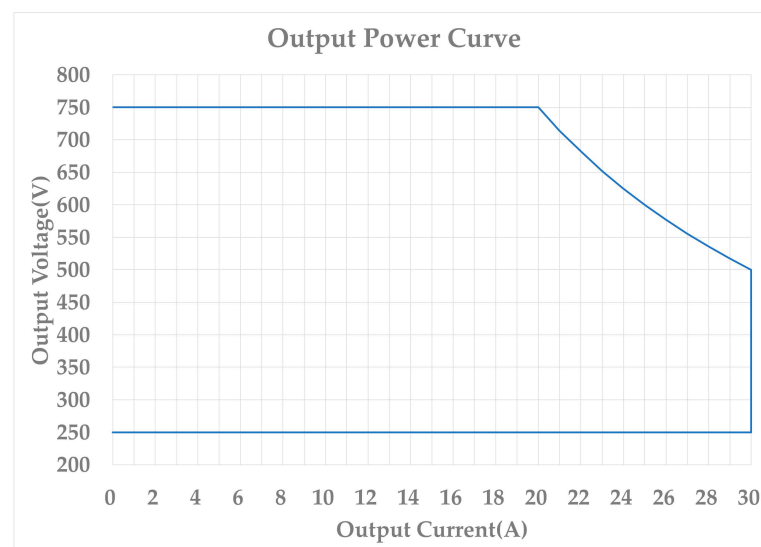


Figure 10. Output voltage–current curve.

5.1. Result of Soft-Start and Transient Response

Firstly, the output voltage is 250 V as the test condition, and the soft start will establish the output voltage smoothly without causing sudden inductor current change. This ensures the stability of the control loop and the effectiveness of the soft start. The simulation result is depicted in Figure 11, while the experimental result is presented in Figure 12.

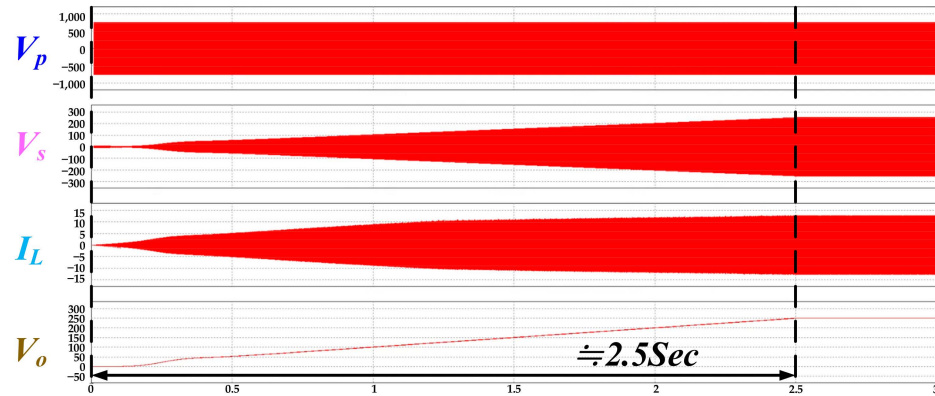


Figure 11. Simulation waveform of TPS soft start with $V_o = 250$ V (V_p : 500 V/div; V_s : 100 V/div; I_L : 5 A/div; time: 500 ms/div).

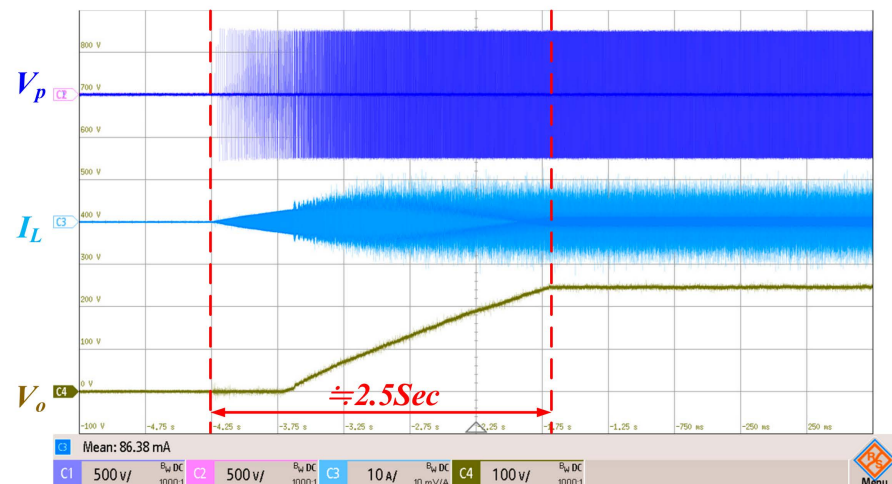


Figure 12. Experimental waveform of TPS soft start with $V_o = 250$ V (V_p : 500 V/div; I_L : 10 A/div; time: 500 ms/div).

Load variation measurements were conducted to verify closed-loop performance and circuit stability within the test conditions ranging from 4.5 kW to 7.5 kW. The comparison of simulated and experimental waveforms aimed to assess the alignment of differences and trends in small-signal modeling and practical measurements appropriately. The results are shown in Figures 13 and 14, respectively.

Next, the output voltage is 750 V as the test condition, the soft start will establish the output voltage smoothly without causing sudden inductor current change. The simulation result is depicted in Figure 15, while the experimental result is presented in Figure 16.

Load variation measurements were also conducted to verify closed-loop performance and circuit stability within the test conditions ranging from 7.5 kW to 15 kW. The comparison of simulated and experimental waveforms aimed to assess the alignment of differences and trends in small-signal modeling and practical measurements appropriately. The results are shown in Figures 17 and 18, respectively.

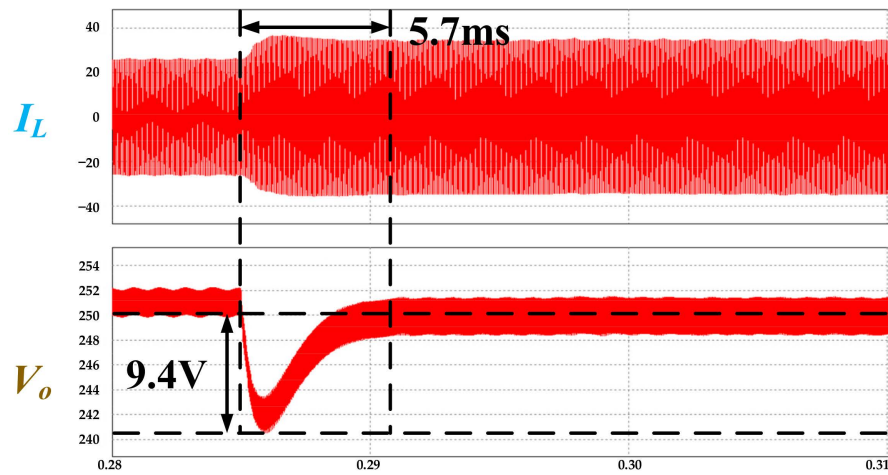


Figure 13. Simulation waveform of TPS load variation from 4.5 kW to 7.5 kW ($V_o = 250$ V) (I_L : 20 A/div, V_o : 2 V/div; time: 10 ms/div).

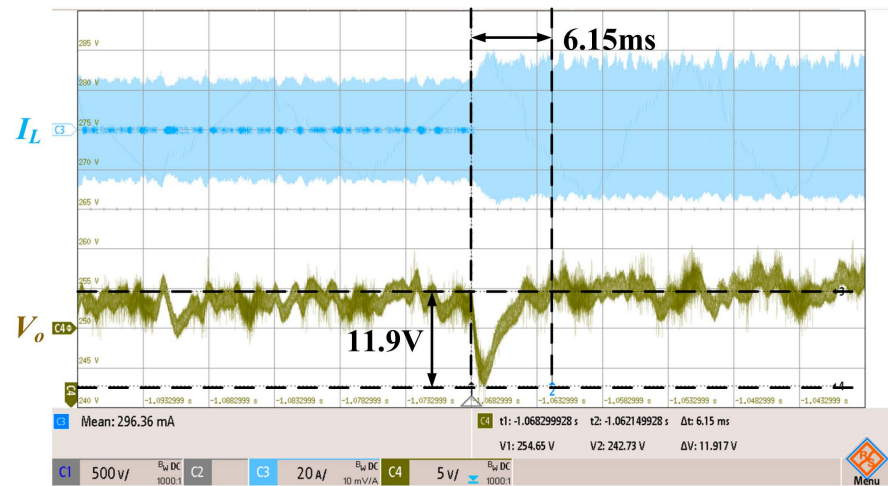


Figure 14. Experimental waveform of TPS load variation from 4.5 kW to 7.5 kW ($V_o = 250$ V) (I_L : 20 A/div, V_o : 5 V/div; time: 5 ms/div).

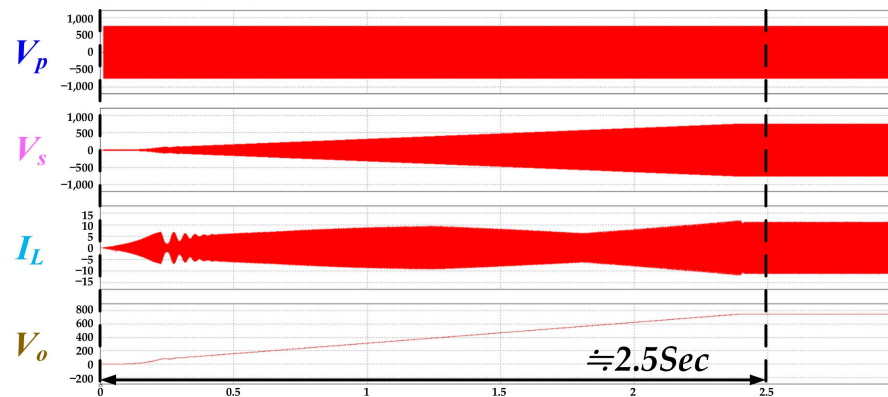


Figure 15. Simulation waveform of TPS soft start with $V_o = 750$ V (V_p : 500 V/div; V_s : 100 V/div; I_L : 5 A/div; time: 500 ms/div).

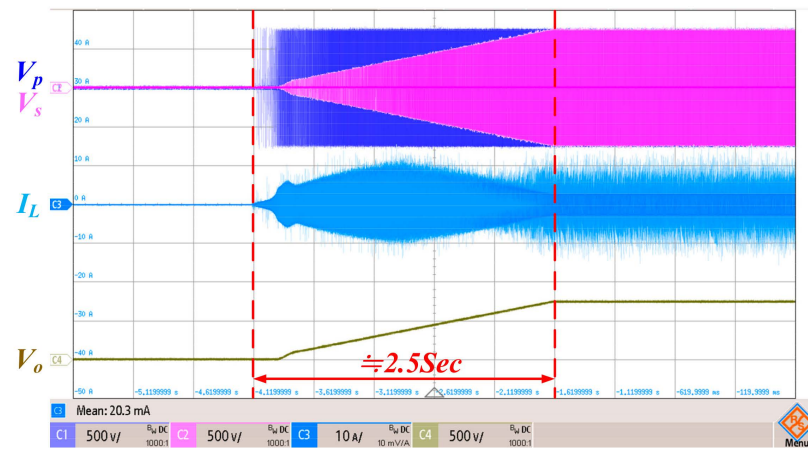


Figure 16. Experimental waveform of TPS soft start with $V_o = 750$ V (V_p : 500 V/div; V_s : 100 V/div; I_L : 5 A/div; time: 500 ms/div).

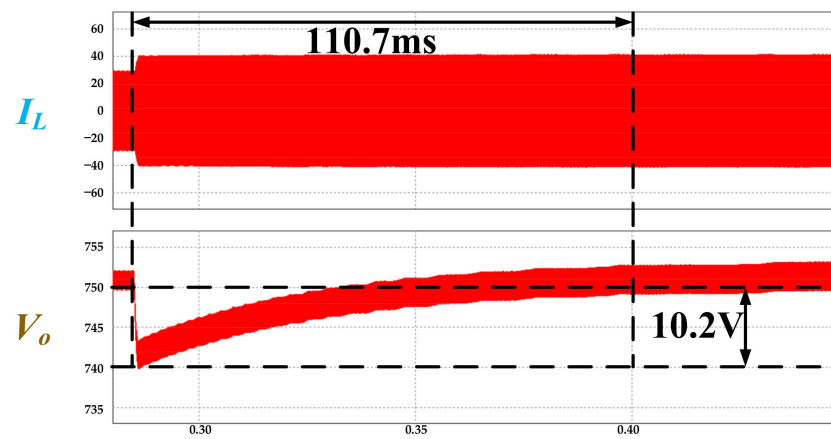


Figure 17. Simulation waveform of TPS load variation from 7.5 kW to 15 kW ($V_o = 750$ V) (I_L : 20 A/div; V_o : 5 V/div; time: 50 ms/div).

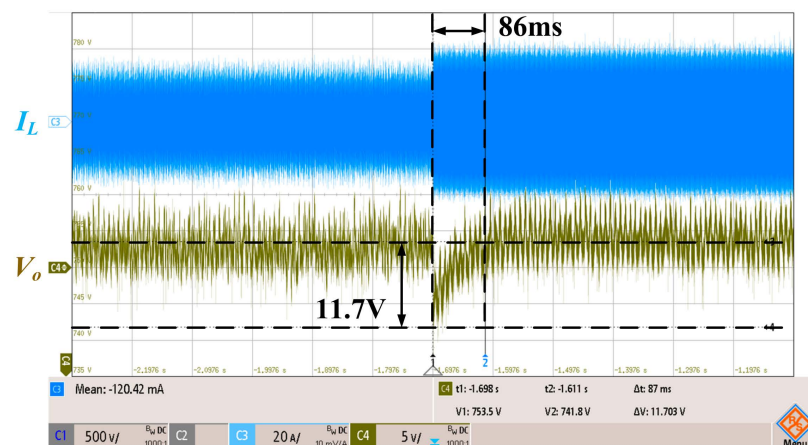


Figure 18. Experimental waveform of TPS load variation from 7.5 kW to 15 kW ($V_o = 750$ V) (I_L : 20 A/div; V_o : 5 V/div; time: 100 ms/div).

5.2. Switching Waveform Comparison of SPS and TPS

TPS modulation controls multiple current transitions. For example, for the primary side voltage V_p from the Lo to Hi state t_{1LH} , the inductor current must be sufficiently negative to achieve the ZVS of Q_1 and Q_2 . For the secondary side voltage V_s from the Lo

to Hi state t_{2LH} , the inductor current must be sufficiently positive to achieve the ZVS of Q_5 and Q_6 . For V_p from the Hi to Lo state t_{1HL} , the inductor current must be sufficiently positive to achieve the ZVS of Q_3 and Q_4 , and for V_s from the Hi to Lo state t_{2HL} , the inductor current must be sufficiently negative to achieve the ZVS of Q_7 and Q_8 . However, all these operations must be established to realize ZVS. When the output power increase, the Minimum Peak Current control will take over. In Figure 19, the experimental of TPS modulation waveform corresponds to a 250 V output, while Figure 20 represents a 750 V output. Each of these waveforms illustrates the switching current points under light load and heavy load conditions, respectively.

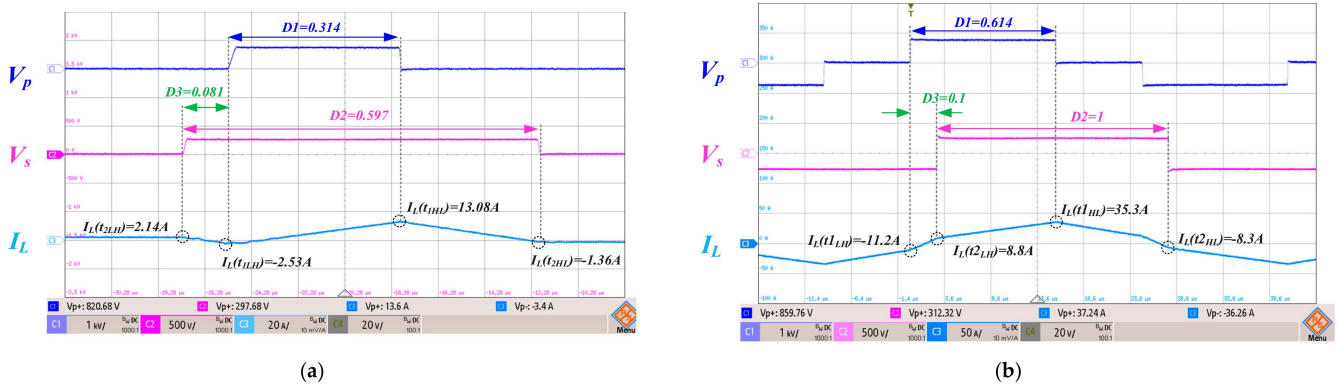


Figure 19. TPS Waveform of $V_o = 250$ V. (a) 1 kW (Case2, SM1), (b) 7.5 kW (Case2, SM3*) (V_p : 1 kV/div; V_s : 500 V/div; I_L : 20 A/div in (a), I_L : 50 A/div in (b), time: 2 μ s/div).

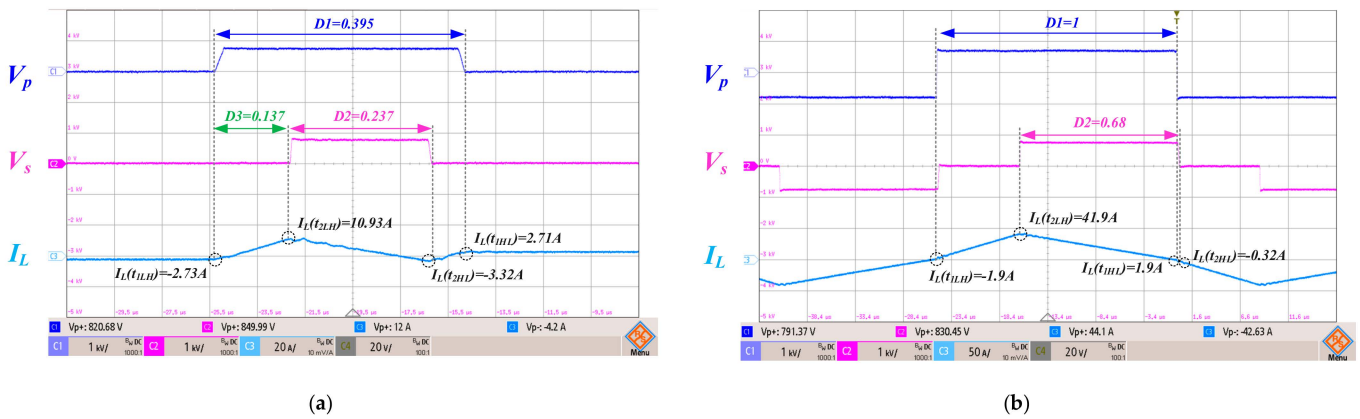
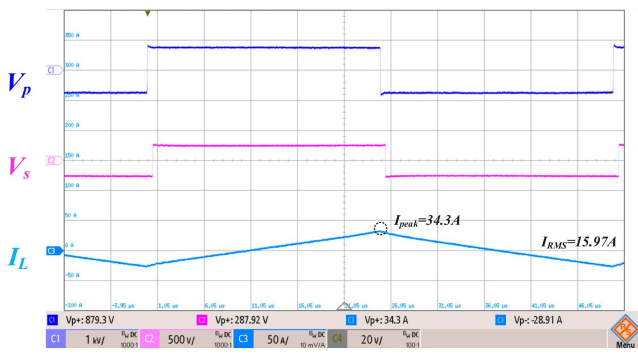
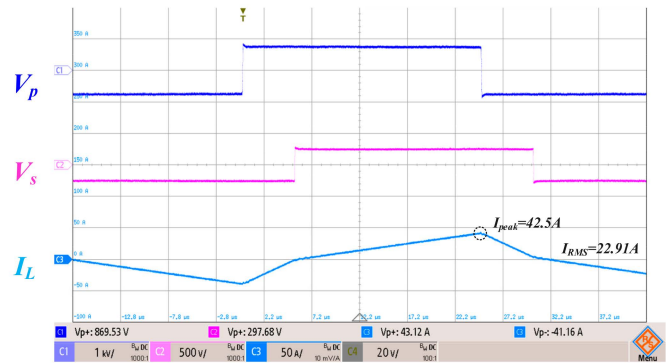


Figure 20. TPS Waveform of $V_o = 750$ V. (a) 1 kW (Case1, SM1), (b) 15 kW (Case1, SM3*) (V_p/V_s : 1 kV/div; I_L : 20 A/div in (a), I_L : 50 A/div in (b), time: 2 μ s/div).

Compared with TPS, SPS modulation only controls the phase shift angle between the primary and secondary sides, which will generate redundant current, thereby causing enormous switching loss at light loads and unnecessary RMS or peak current at heavy loads. In Figure 21, the experimental of SPS modulation waveform corresponds to a 250 V output, while Figure 22 represents a 750 V output. Each of these waveforms illustrates the switching current points under light load and heavy load conditions, respectively.



(a)

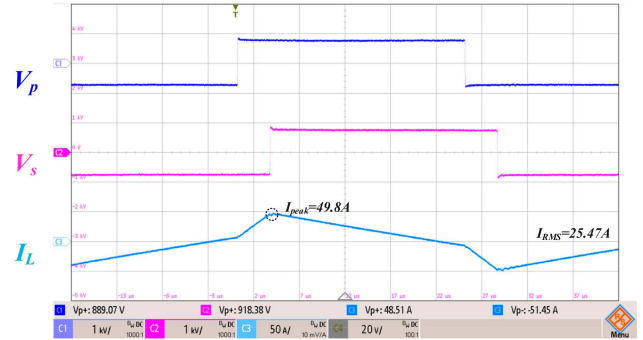


(b)

Figure 21. SPS Waveform of $V_o = 250$ V. (a) 1 kW, (b) 7.5 kw (V_p : 1 kV/div; V_s : 500 V/div; I_L : 50 A/div; time: 5 μ s/div).



(a)

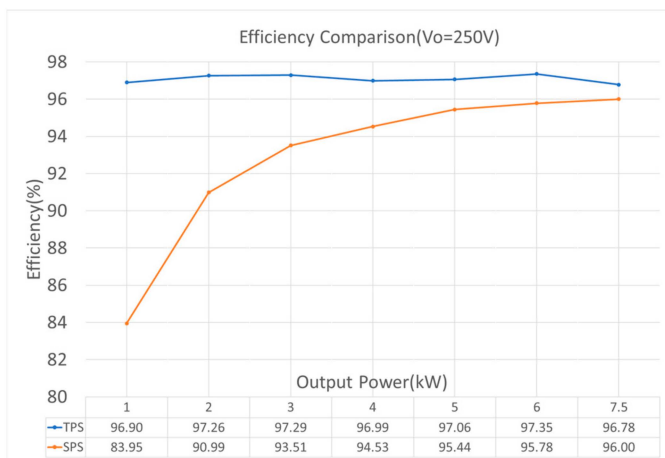


(b)

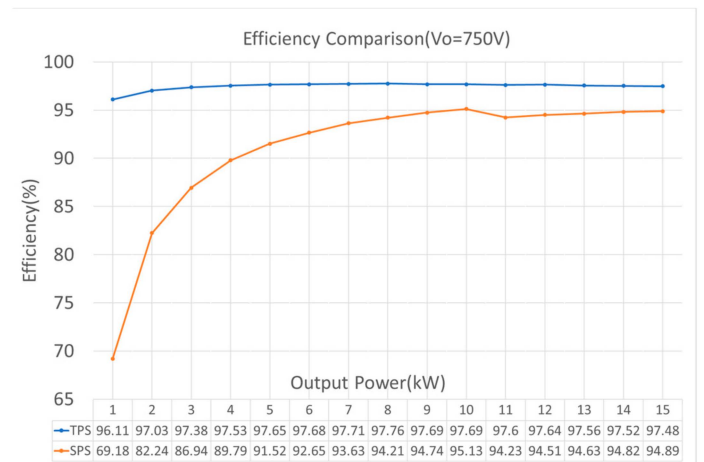
Figure 22. SPS Waveform of $V_o = 750$ V. (a) 1 kW, (b) 15 kW (V_p/V_s : 1 kV/div; I_L : 50 A/div; time: 5 μ s/div).

5.3. Efficiency Comparison

Figure 23 shows the measured efficiency curves at output voltage conditions of 250 and 750 V. High efficiency performance can be achieved at a wide range of output voltages.



(a)



(b)

Figure 23. Measured efficiency curves at (a) 250 V and (b) 750 V output voltage conditions.

6. Conclusions

In this paper, we present a high-efficiency dual-active-bridge converter with an optimal control method using triple-phase-shift (TPS) modulation for the battery charger of electric vehicles. This approach eliminates switching losses through an ALL-ZVS mode under light loads and improves conduction losses through Minimum Peak Current mode once the load current is sufficient to allow all switches to enter ZVS. Additionally, we address and propose Ambiguous mode to resolve issues arising at the boundary between these two modes. Based on the above, this research simplifies controller's calculations and reduces analysis workload by offering a convergent approach to determine the number of TPS operation modes (*Case 1 SM1*, *Case 1 SM3**, *Case 2 SM1* and *Case 2 SM3**) that necessitate analysis within the small-signal model. It also ensures the circuit's stability when operating under these selected modes, that it is accurately modeled by GAM, and that the derived results are verified through simulation and experiment. Finally, a 15 kW test platform is used to validate the design. The soft-start function, transient response, and TPS and SPS modulation efficiency comparison are presented. Finally, this platform achieves 97.71% and 97.76% efficiencies at 250 V/7.5 kW and 750 V/8 kW, respectively, which obtained 26.93% and 2.59% efficiency improvement at 750 V/1 kW and 750 V/15 kW through the All-ZVS mode and the Minimum Peak Current mode, respectively.

Author Contributions: Conceptualization, S.-h.K.; Methodology, T.-W.H.; Software, C.-W.C.; Investigation, C.-W.C.; Data curation, S.-h.K. and Y.-C.C.; Writing—original draft, S.-h.K. and Y.-C.C.; Writing—review & editing, S.-h.K., H.-J.C., S.B., S.P., M.J. and M.T.; Visualization, S.B., S.P., M.J. and M.T.; Supervision, H.-J.C., T.-W.H. and Y.-C.C.; Project administration, H.-J.C. and T.-W.H. All authors have read and agreed to the published version of the manuscript.

Funding: This research received no external funding.

Data Availability Statement: Data are contained within the article.

Conflicts of Interest: The authors declare no conflict of interest.

Appendix A

The detailed small-signal coefficient terms of the variables in each Equations (15)–(19) have been arranged to correspond to (A1) to (A5) for matrices A , B , C and D .

$$\begin{aligned} \frac{d}{dt} \Delta i_{L_{1R}} = & \Delta i_{L_{1R}} \times \frac{-R_t}{L_t} \\ & + \Delta i_{L_{1I}} \times \omega_s \\ & + \Delta v_{in_0} \times \frac{\sin(2\pi D_1)}{\pi L_t} \\ & + \Delta v_{o_0} \times \frac{-N}{\pi L_t} [\sin[\pi(D_1 + D_2 + 2D_\varphi)] - \sin[\pi(D_1 - D_2 + 2D_\varphi)]] \\ & + \Delta d_1 \times \frac{1}{L_t} \left[\begin{aligned} & 2 \cos(2\pi D_1) \times V_{in_0} \\ & - NV_{o_0} \times [\cos[\pi(D_1 + D_2 + 2D_\varphi)] - \cos[\pi(D_1 - D_2 + 2D_\varphi)]] \end{aligned} \right] \\ & + \Delta d_2 \times \frac{-N}{L_t} [V_{o_0} \times [\cos[\pi(D_1 + D_2 + 2D_\varphi)] + \cos[\pi(D_1 - D_2 + 2D_\varphi)]]] \\ & + \Delta d_\varphi \times \frac{-N}{L_t} [2V_{o_0} \times [\cos[\pi(D_1 + D_2 + 2D_\varphi)] - \cos[\pi(D_1 - D_2 + 2D_\varphi)]]] \end{aligned} \quad (A1)$$

$$\begin{aligned} \frac{d}{dt} \Delta i_{L_{1I}} = & \Delta i_{L_{1R}} \times (-\omega_s) \\ & + \Delta i_{L_{1I}} \times \frac{-R_t}{L_t} \\ & + \Delta v_{in_0} \times \frac{\cos(2\pi D_1) - 1}{\pi L_t} \\ & + \Delta v_{o_0} \times \frac{-N}{\pi L_t} [\cos[\pi(D_1 + D_2 + 2D_\varphi)] - \cos[\pi(D_1 - D_2 + 2D_\varphi)]] \\ & + \Delta d_1 \times \frac{-1}{L_t} \left[\begin{aligned} & 2 \sin(2\pi D_1) \times V_{in_0} \\ & + NV_{o_0} \times [\sin[\pi(D_1 - D_2 + 2D_\varphi)] - \sin[\pi(D_1 + D_2 + 2D_\varphi)]] \end{aligned} \right] \\ & + \Delta d_2 \times \frac{-N}{L_t} [V_{o_0} \times [-\sin[\pi(D_1 + D_2 + 2D_\varphi)] - \sin[\pi(D_1 - D_2 + 2D_\varphi)]]] \\ & + \Delta d_\varphi \times \frac{-N}{L_t} [2V_{o_0} \times [\sin[\pi(D_1 - D_2 + 2D_\varphi)] - \sin[\pi(D_1 + D_2 + 2D_\varphi)]]] \end{aligned} \quad (A2)$$

$$\begin{aligned}
\frac{d}{dt} \Delta v_{c_0} = & \Delta i_{N_0} \times \frac{-R}{C_o(R+r_c)} \\
& + \Delta v_{c_0} \times \frac{-1}{C_o(R+r_c)} \\
& + \Delta i_{L_{1R}} \times \frac{2NR}{\pi C_o(R+r_c)} [\sin[\pi(D_1 + D_2 + 2D_\varphi)] - \sin[\pi(D_1 - D_2 + 2D_\varphi)]] \\
& + \Delta i_{L_{1I}} \times \frac{2NR}{\pi C_o(R+r_c)} [\cos[\pi(D_1 + D_2 + 2D_\varphi)] - \cos[\pi(D_1 - D_2 + 2D_\varphi)]] \\
& + \Delta d_1 \times \frac{2NR}{C_o(R+r_c)} \left[\begin{array}{l} I_{L_{1R}} \times [\cos[\pi(D_1 + D_2 + 2D_\varphi)] - \cos[\pi(D_1 - D_2 + 2D_\varphi)]] \\ + I_{L_{1I}} \times [\sin[\pi(D_1 - D_2 + 2D_\varphi)] - \sin[\pi(D_1 + D_2 + 2D_\varphi)]] \end{array} \right] \\
& + \Delta d_2 \times \frac{2NR}{C_o(R+r_c)} \left[\begin{array}{l} I_{L_{1R}} \times [\cos[\pi(D_1 + D_2 + 2D_\varphi)] + \cos[\pi(D_1 - D_2 + 2D_\varphi)]] \\ - I_{L_{1I}} \times [\sin[\pi(D_1 + D_2 + 2D_\varphi)] + \sin[\pi(D_1 - D_2 + 2D_\varphi)]] \end{array} \right] \\
& + \Delta d_\varphi \times \frac{2NR}{C_o(R+r_c)} \left[\begin{array}{l} 2I_{L_{1R}} \times [\cos[\pi(D_1 + D_2 + 2D_\varphi)] - \cos[\pi(D_1 - D_2 + 2D_\varphi)]] \\ + 2I_{L_{1I}} \times [\sin[\pi(D_1 - D_2 + 2D_\varphi)] - \sin[\pi(D_1 + D_2 + 2D_\varphi)]] \end{array} \right]
\end{aligned} \tag{A3}$$

$$\begin{aligned}
\frac{d}{dt} \Delta v_{o_0} = & \Delta i_{N_0} \times \frac{-R \times r_c}{R+r_c} \\
& + \Delta v_{c_0} \times \frac{R}{R+r_c} \\
& + \Delta i_{L_{1R}} \times \frac{2NRr_c}{\pi(R+r_c)} [\sin[\pi(D_1 + D_2 + 2D_\varphi)] - \sin[\pi(D_1 - D_2 + 2D_\varphi)]] \\
& + \Delta i_{L_{1I}} \times \frac{2NRr_c}{\pi(R+r_c)} [\cos[\pi(D_1 + D_2 + 2D_\varphi)] - \cos[\pi(D_1 - D_2 + 2D_\varphi)]] \\
& + \Delta d_1 \times \frac{2NRr_c}{R+r_c} \left[\begin{array}{l} I_{L_{1R}} \times [\cos[\pi(D_1 + D_2 + 2D_\varphi)] - \cos[\pi(D_1 - D_2 + 2D_\varphi)]] \\ + I_{L_{1I}} \times [\sin[\pi(D_1 - D_2 + 2D_\varphi)] - \sin[\pi(D_1 + D_2 + 2D_\varphi)]] \end{array} \right] \\
& + \Delta d_2 \times \frac{2NRr_c}{R+r_c} \left[\begin{array}{l} I_{L_{1R}} \times [\cos[\pi(D_1 + D_2 + 2D_\varphi)] + \cos[\pi(D_1 - D_2 + 2D_\varphi)]] \\ - I_{L_{1I}} \times [\sin[\pi(D_1 + D_2 + 2D_\varphi)] + \sin[\pi(D_1 - D_2 + 2D_\varphi)]] \end{array} \right] \\
& + \Delta d_\varphi \times \frac{2NRr_c}{R+r_c} \left[\begin{array}{l} 2I_{L_{1R}} \times [\cos[\pi(D_1 + D_2 + 2D_\varphi)] - \cos[\pi(D_1 - D_2 + 2D_\varphi)]] \\ + 2I_{L_{1I}} \times [\sin[\pi(D_1 - D_2 + 2D_\varphi)] - \sin[\pi(D_1 + D_2 + 2D_\varphi)]] \end{array} \right]
\end{aligned} \tag{A4}$$

$$\begin{aligned}
\frac{d}{dt} \Delta i_{o_0} = & \Delta i_{N_0} \times \frac{R}{R+r_c} \\
& + \Delta v_{c_0} \times \frac{1}{R+r_c} \\
& + \Delta i_{L_{1R}} \times \frac{2Nr_c}{\pi(R+r_c)} [\sin[\pi(D_1 + D_2 + 2D_\varphi)] - \sin[\pi(D_1 - D_2 + 2D_\varphi)]] \\
& + \Delta i_{L_{1I}} \times \frac{2Nr_c}{\pi(R+r_c)} [\cos[\pi(D_1 + D_2 + 2D_\varphi)] - \cos[\pi(D_1 - D_2 + 2D_\varphi)]] \\
& + \Delta d_1 \times \frac{2Nr_c}{R+r_c} \left[\begin{array}{l} I_{L_{1R}} \times [\cos[\pi(D_1 + D_2 + 2D_\varphi)] - \cos[\pi(D_1 - D_2 + 2D_\varphi)]] \\ + I_{L_{1I}} \times [\sin[\pi(D_1 - D_2 + 2D_\varphi)] - \sin[\pi(D_1 + D_2 + 2D_\varphi)]] \end{array} \right] \\
& + \Delta d_2 \times \frac{2Nr_c}{R+r_c} \left[\begin{array}{l} I_{L_{1R}} \times [\cos[\pi(D_1 + D_2 + 2D_\varphi)] + \cos[\pi(D_1 - D_2 + 2D_\varphi)]] \\ - I_{L_{1I}} \times [\sin[\pi(D_1 + D_2 + 2D_\varphi)] + \sin[\pi(D_1 - D_2 + 2D_\varphi)]] \end{array} \right] \\
& + \Delta d_\varphi \times \frac{2Nr_c}{R+r_c} \left[\begin{array}{l} 2I_{L_{1R}} \times [\cos[\pi(D_1 + D_2 + 2D_\varphi)] - \cos[\pi(D_1 - D_2 + 2D_\varphi)]] \\ + 2I_{L_{1I}} \times [\sin[\pi(D_1 - D_2 + 2D_\varphi)] - \sin[\pi(D_1 + D_2 + 2D_\varphi)]] \end{array} \right]
\end{aligned} \tag{A5}$$

References

1. Acharige, S.S.G.; Haque, M.E.; Arif, M.T.; Hosseinzadeh, N.; Hasan, K.N.; Oo, A.M.T. Review of Electric Vehicle Charging Technologies, Standards, Architectures, and Converter Configurations. *IEEE Access* **2023**, *11*, 41218–41255. [\[CrossRef\]](#)
2. Safayatullah, M.; Elrais, M.T.; Ghosh, S.; Rezaii, R.; Batarseh, I. A Comprehensive Review of Power Converter Topologies and Control Methods for Electric Vehicle Fast Charging Applications. *IEEE Access* **2022**, *10*, 40753–40793. [\[CrossRef\]](#)
3. Shurrab, M.; Singh, S.; Otok, H.; Mizouni, R.; Khadkikar, V.; Zeineldin, H. An Efficient Vehicle-to-Vehicle (V2V) Energy Sharing Framework. *IEEE Internet Things J.* **2022**, *9*, 5315–5328. [\[CrossRef\]](#)
4. Haque, M.M.; Wolfs, P.; Alahakoon, S.; Sturmberg, B.C.P.; Nadarajah, M.; Zare, F. DAB Converter with Q Capability for BESS/EV Applications to Allow V2H/V2G Services. *IEEE Trans. Ind. Appl.* **2022**, *58*, 468–480. [\[CrossRef\]](#)
5. Zayed, O.; Elezab, A.; Abuelnaga, A.; Narimani, M. A Dual-Active Bridge Converter with a Wide Output Voltage Range (200–1000 V) for Ultrafast DC-Connected EV Charging Stations. *IEEE Trans. Transp. Electr.* **2023**, *9*, 3731–3741. [\[CrossRef\]](#)
6. Assadi, S.A.; Matsumoto, H.; Moshirvaziri, M.; Nasr, M.; Zaman, M.S.; Trescases, O. Active saturation mitigation in high-density dual-active-bridge DC–DC converter for on-board EV charger applications. *IEEE Trans. Power Electron.* **2019**, *35*, 4376–4387. [\[CrossRef\]](#)
7. Choi, H.-J.; Jung, J.-H. Practical design of dual active bridge converter as isolated bi-directional power interface for solid state transformer applications. *J. Electr. Eng. Technol.* **2016**, *11*, 1265–1273. [\[CrossRef\]](#)

8. Fontes, G.; Turpin, C.; Astier, S.; Meynard, T.A. Interactions between fuel cells and power converters: Influence of current harmonics on a fuel cell stack. *IEEE Trans. Power Electron.* **2007**, *22*, 670–678. [[CrossRef](#)]
9. Ehsani, M.; Singh, K.V.; Bansal, H.O.; Mehrjardi, R.T. State of the Art and Trends in Electric and Hybrid Electric Vehicles. *Proc. IEEE* **2021**, *109*, 967–984. [[CrossRef](#)]
10. Tu, H.; Feng, H.; Srdic, S.; Lukic, S. Extreme Fast Charging of Electric Vehicles: A Technology Overview. *IEEE Trans. Transp. Electrification* **2019**, *5*, 861–878. [[CrossRef](#)]
11. Schmid, J.; Strauss, P.; Hatzigiorgiou, N.; Akkermans, H.; Buchholz, B.; Van Oostvoorn, F.; Scheepers, M.; Reyero, R.; Chadjivassiliadis, J. *Towards Smart Power Networks: Lessons Learned from European Research FP5 Projects*; European Commission Directorate-General for Research Information and Communication Unit: Brussels, Belgium, 2005.
12. Barone, G.; Brusco, G.; Burgio, A.; Motta, M.; Menniti, D.; Pinnarelli, A.; Sorrentino, N. A dual active bridge dc-dc converter for application in a smart user network. In Proceedings of the 2014 Australasian Universities Power Engineering Conference (AUPEC), Perth, WA, Australia, 28 September–1 October 2014; pp. 1–5.
13. Manez, K.T. Advances in bidirectional DC-DC converters for future energy systems. Ph.D. Thesis, Technical University of Denmark, Lyngby, Denmark, 2018.
14. Xue, L.; Shen, Z.; Boroyevich, D.; Mattavelli, P.; Diaz, D. Dual active bridge-based battery charger for plug-in hybrid electric vehicle with charging current containing low frequency ripple. *IEEE Trans. Power Electron.* **2015**, *30*, 7299–7307. [[CrossRef](#)]
15. Mathew, A.; Prasad, U.R.; Madhu, G.M.; Naik, N.; Vjayanathi, C.; Subudhi, B. Performance Analysis of a Dual Active Bridge Converter in EV Charging Applications. In Proceedings of the 2022 International Conference for Advancement in Technology (ICONAT), Goa, India, 21–22 January 2022; pp. 1–6.
16. Bai, H.; Mi, C. Eliminate Reactive Power and Increase System Efficiency of Isolated Bidirectional Dual-Active-Bridge DC-DC Converters Using Novel Dual-Phase-Shift Control. *IEEE Trans. Power Electron.* **2008**, *23*, 2905–2914. [[CrossRef](#)]
17. Feng, B.; Wang, Y.; Man, J. A novel dual-phase-shift control strategy for dual-active-bridge DC-DC converter. In Proceedings of the IECON 2014—40th Annual Conference of the IEEE Industrial Electronics Society, Dallas, TX, USA, 29 October–1 November 2014; pp. 4140–4145.
18. Shao, S.; Jiang, M.; Ye, W.; Li, Y.; Zhang, J.; Sheng, K. Optimal Phase-Shift Control to Minimize Reactive Power for a Dual Active Bridge DC-DC Converter. *IEEE Trans. Power Electron.* **2019**, *34*, 10193–10205. [[CrossRef](#)]
19. Zhao, B.; Song, Q.; Liu, W.; Sun, Y. Overview of Dual-Active-Bridge Isolated Bidirectional DC-DC Converter for High-Frequency-Link Power-Conversion System. *IEEE Trans. Power Electron.* **2014**, *29*, 4091–4106. [[CrossRef](#)]
20. Zhao, B.; Yu, Q.; Sun, W. Extended-Phase-Shift Control of Isolated Bidirectional DC-DC Converter for Power Distribution in Microgrid. *IEEE Trans. Power Electron.* **2012**, *27*, 4667–4680. [[CrossRef](#)]
21. Huang, J.; Wang, Y.; Li, Z.; Lei, W. Unified Triple-Phase-Shift Control to Minimize Current Stress and Achieve Full Soft-Switching of Isolated Bidirectional DC-DC Converter. *IEEE Trans. Ind. Electron.* **2016**, *63*, 4169–4179. [[CrossRef](#)]
22. Middlebrook, R.D.; Cuk, S. A general unified approach to modelling switching-converter power stages. In Proceedings of the 1976 IEEE Power Electronics Specialists Conference, Cleveland, OH, USA, 8–10 June 1976; pp. 18–34.
23. Das, D.; Mishra, S.; Singh, B. Design Architecture for Continuous-Time Control of Dual Active Bridge Converter. *IEEE J. Emerg. Sel. Top. Power Electron.* **2021**, *9*, 3287–3295. [[CrossRef](#)]
24. Hiltunen, J.; Väisänen, V.; Juntunen, R.; Silventoinen, P. Variable-frequency phase shift modulation of a dual active bridge converter. *IEEE Trans. Power Electron.* **2015**, *30*, 7138–7148. [[CrossRef](#)]
25. van Hoek, H.; Neubert, M.; De Doncker, R.W. Enhanced modulation strategy for a three-phase dual active bridge—Boosting efficiency of an electric vehicle converter. *IEEE Trans. Power Electron.* **2013**, *28*, 5499–5507. [[CrossRef](#)]
26. Krismer, F.; Kolar, J.W. Accurate power loss model derivation of a high-current dual active bridge converter for an automotive application. *IEEE Trans. Ind. Electron.* **2009**, *57*, 881–891. [[CrossRef](#)]
27. Calderon, C.; Barrado, A.; Rodriguez, A.; Alou, P.; Lazaro, A.; Fernandez, C.; Zumel, P. General analysis of switching modes in a dual active bridge with triple phase shift modulation. *Energies* **2018**, *11*, 2419. [[CrossRef](#)]
28. Bacha, S.; Munteanu, I.; Bratcu, A.I. Power electronic converters modeling and control. *Adv. Textb. Control Signal Process.* **2014**, *454*, 454.
29. Iqbal, M.T.; Maswood, A.I. An explicit discrete-time large-and small-signal modeling of the dual active bridge DC-DC converter based on the time scale methodology. *IEEE J. Emerg. Sel. Top. Ind. Electron.* **2021**, *2*, 545–555. [[CrossRef](#)]
30. Safayatullah, M.; Batarseh, I. Small signal model of dual active bridge converter for multi-phase shift modulation. In Proceedings of the 2020 IEEE Energy Conversion Congress and Exposition (ECCE), Detroit, MI, USA, 11–15 October 2020; pp. 5960–5965.
31. Bu, Q.; Wen, H. Triple-phase-shifted bidirectional full-bridge converter with wide range zvs. In Proceedings of the 2018 IEEE International Conference on Power Electronics, Drives and Energy Systems (PEDES), Chennai, India, 18–21 December 2018; pp. 1–6.
32. Chen, Y.-H.; Huang, T.-W.; Kuo, S.-H.; Chang, Y.-C.; Chiu, H.-J.; Bachman, S.; Jasiński, M. Dual-Active-Bridge Converter with Triple Phase Shift Control for a Wide Operating Voltage Range. In Proceedings of the 2023 11th International Conference on Power Electronics and ECCE Asia (ICPE 2023-ECCE Asia), Jeju, Republic of Korea, 22–25 May 2023; pp. 1752–1755.

33. Qin, H.; Kimball, J.W. Generalized average modeling of dual active bridge DC–DC converter. *IEEE Trans. Power Electron.* **2011**, *27*, 2078–2084.
34. Sanders, S.R.; Noworolski, J.M.; Liu, X.Z.; Verghese, G.C. Generalized averaging method for power conversion circuits. *IEEE Trans. Power Electron.* **1991**, *6*, 251–259. [[CrossRef](#)]

Disclaimer/Publisher’s Note: The statements, opinions and data contained in all publications are solely those of the individual author(s) and contributor(s) and not of MDPI and/or the editor(s). MDPI and/or the editor(s) disclaim responsibility for any injury to people or property resulting from any ideas, methods, instructions or products referred to in the content.